Characterization of NiFe oxyhydroxide electrocatalysts by integrated electronic structure calculations and spectroelectrochemistry

Zachary K. Goldsmith[a], Aparna K. Harshan[a], James B. Gerken[b], Márton Vörös[c,d], Giulia Galli[c,d,1], Shannon S. Stahl[b,1], and Sharon Hammes-Schiffer[a,1]

[a]Department of Chemistry, University of Illinois at Urbana–Champaign, Urbana, IL 61801; [b]Department of Chemistry, University of Wisconsin–Madison, Madison, WI 53706; [c]Institute for Molecular Engineering, University of Chicago, Chicago, IL 60637; and [d]Argonne National Laboratory, Lemont, IL 60439

Contributed by Sharon Hammes-Schiffer, February 7, 2017 (sent for review December 24, 2016; reviewed by Shannon W. Boettcher and Annabella Selloni)

NiFe oxyhydroxide materials are highly active electrocatalysts for the oxygen evolution reaction (OER), an important process for carbon-neutral energy storage. Recent spectroscopic and computational studies increasingly support iron as the site of catalytic activity but differ with respect to the relevant iron redox state. A combination of hybrid periodic density functional theory calculations and spectroelectrochemical experiments elucidate the electronic structure and redox thermodynamics of Ni-only and mixed NiFe oxyhydroxide thin-film electrocatalysts. The UV/visible light absorbance of the Ni-only catalyst depends on the applied potential as metal ions in the film are oxidized before the onset of OER activity. In contrast, absorbance changes are negligible in a 25% Fe-doped catalyst up to the onset of OER activity. First-principles calculations of proton-coupled redox potentials and magnetizations reveal that the Ni-only system features oxidation of Ni^{2+} to Ni^{3+}, followed by oxidation to a mixed $Ni^{3+/4+}$ state at a potential coincident with the onset of OER activity. Calculations on the 25% Fe-doped system show the catalyst is redox inert before the onset of catalysis, which coincides with the formation of Fe^{4+} and mixed Ni oxidation states. The calculations indicate that introduction of Fe dopants changes the character of the conduction band minimum from Ni-oxide in the Ni-only to predominantly Fe-oxide in the NiFe electrocatalyst. These findings provide a unified experimental and theoretical description of the electrochemical and optical properties of Ni and NiFe oxyhydroxide electrocatalysts and serve as an important benchmark for computational characterization of mixed-metal oxidation states in heterogeneous catalysts.

NiFe oxyhydroxide | oxygen evolution reaction | electrocatalysis | spectroelectrochemistry | density functional theory

The photoelectrochemical conversion of water into O_2 and H_2 is a major focus of energy storage and conversion efforts (1–4), with significant attention directed toward development of efficient catalysts for water oxidation and reduction. Such catalysts should operate at low overpotential, exhibit high selectivity, and be composed of earth-abundant materials. Commercial electrolyzers typically use transition-metal-oxide electrocatalysts for the oxygen evolution reaction (OER) (5, 6), and nickel, nickel–iron, and other mixed-metal oxides are especially effective under alkaline conditions (7, 8). Despite the importance and potential future impact of these materials, many features of their catalytic mechanism are poorly understood.

Nickel oxyhydroxide has long been associated with OER electrocatalysis (9, 10); however, much of the activity in this material has been shown to arise from the presence of Fe impurities (7, 11). This conclusion complements extensive independent studies demonstrating the effectiveness of NiFe-based oxide and oxyhydroxide materials as OER electrocatalysts (12–14), including a survey of nearly 3,500 mixed-metal-oxide compositions, which drew attention to the high electrocatalytic activity of materials containing Ni, Fe, and a third metal (e.g., Ba, Sr, Ca, or Cr) (15). Such observations account for the extensive interest in understanding the structural and mechanistic principles underlying the high activity of NiFe-based electrocatalysts.

A recent combined experimental and computational study investigated Ni-, Fe-, and various NiFe-oxyhydroxide-based electrocatalysts in an effort to probe the redox behavior and electrocatalytic mechanism of these catalysts (16). *Operando* X-ray absorption spectroscopy and density functional theory calculations with the Hubbard U correction (DFT+U) implicated the presence of Fe^{3+} sites within NiFe oxyhydroxide as the active site for O–O bond formation (17). The formation or catalytic role of Fe^{4+} or other high-valent Fe species was disfavored based on the experimental and computational data. A subsequent *operando* Mössbauer spectroscopic study, however, showed that significant quantities of Fe^{4+} are generated in NiFe-oxyhydroxide catalysts during electrocatalytic water oxidation (18), and the accessibility of Fe^{4+} was supported by an independent computational study of such materials (19). These different, and sometimes conflicting, observations highlight the need for an improved understanding of complex materials of this type, ideally drawing upon synergistic contributions from experimental and computational approaches.

Herein, we report a theoretical and spectroelectrochemical study of Ni and 25% Fe-doped Ni oxyhydroxide electrocatalysts. Cyclic voltammetry and hybrid DFT calculations were used to

Significance

The conversion of water to oxygen and hydrogen molecules is essential for a variety of renewable energy technologies. Nickel–iron (NiFe) oxyhydroxide is an important, earth-abundant electrocatalyst for the oxygen evolution reaction. A combined experimental and computational study of pure Ni oxyhydroxide and mixed NiFe oxyhydroxide thin films elucidates the chemistry governing their different electrochemical and optical properties. The Ni and Fe oxidation states in each system are assigned as a function of applied potential based on quantum-mechanical calculations, cyclic voltammetry, and UV-visible spectroscopy. In the more catalytically active NiFe system, oxidation to Fe^{4+} coincides with the onset of oxygen evolution. Synergy between experiment and theory provides a detailed, atomistic understanding of this robust catalyst.

Author contributions: Z.K.G., A.K.H., J.B.G., M.V., G.G., S.S.S., and S.H.-S. designed research; Z.K.G., A.K.H., J.B.G., and M.V. performed research; Z.K.G., A.K.H., J.B.G., M.V., G.G., S.S.S., and S.H.-S. analyzed data; and Z.K.G., A.K.H., J.B.G., M.V., G.G., S.S.S., and S.H.-S. wrote the paper.

Reviewers: S.W.B., University of Oregon; and A.S., Princeton University.

The authors declare no conflict of interest.

Freely available online through the PNAS open access option.

[1]To whom correspondence may be addressed. Email: gagalli@uchicago.edu, stahl@chem.wisc.edu, or shs3@illinois.edu.

This article contains supporting information online at www.pnas.org/lookup/suppl/doi:10.1073/pnas.1702081114/-/DCSupplemental.

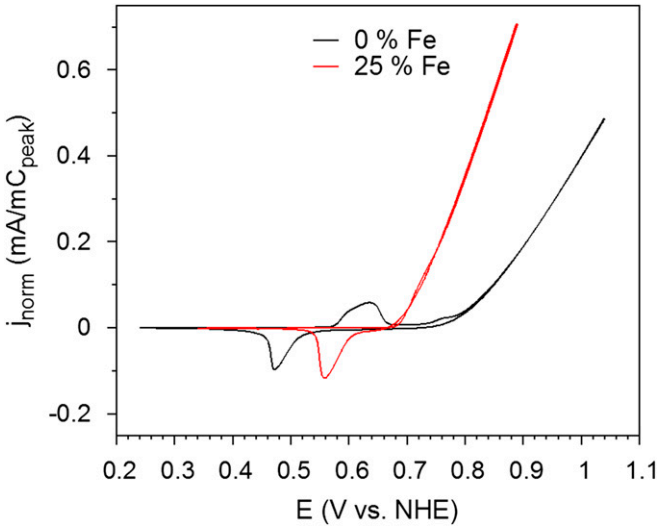

Fig. 1. CVs of $Ni_4O_8H_n$ (black trace) and $Ni_3Fe_1O_8H_n$ (red) films on FTO (fluorine-doped tin oxide) electrodes in 1 M KOH at 5 mV/s. Current densities are normalized to the peak area of the cathodic peak. Data for intermediate Fe loadings are given in *SI Appendix*, Fig. S9.

determine the redox potentials for proton-coupled oxidation of the film and assign relevant metal oxidation states at different applied potentials, including those contributing to catalytic water oxidation. The optoelectronic properties of the pure Ni and Fe-doped catalysts obtained from experiment and computation provide an atomistic description of the dominant states at the valence and conduction band edges. Collectively, the results offer insights into the influence of iron dopants on the redox properties and electronic structure of Ni oxyhydroxide electrocatalysts.

Results and Discussion

Electrochemical Behavior of NiFe Oxyhydroxide in Situ. The present study focuses on a comparison of pure Ni and 25% Fe-doped Ni oxyhydroxide electrocatalysts. To perform experimental studies, thin films of $Ni(OH)_2$ or Fe-doped $Ni(OH)_2$ were prepared via electrodeposition, as elaborated in the *SI Appendix*. Cyclic voltammograms (CVs) of the resulting materials reveal differences in voltammetric responses (Fig. 1), consistent with previous observations (7, 11, 12, 20, 21). The pure Ni material exhibits an isolated $Ni^{2+/3+}$ redox feature in the CV, with a midpoint potential of 0.53 V vs. NHE (normal hydrogen electrode), and a small redox feature (peak potential ~0.76 V) at the foot of the large irreversible wave corresponding to the catalytic OER, which has an onset potential of ~0.72 V. Introduction of iron into the oxide is known to increase the $Ni^{2+/3+}$ potential and decrease the onset potential for catalysis (7, 11, 12, 20, 21). With the 25% Fe-doped material, the two features are fully merged, and only a small shoulder is evident at the foot of the catalytic wave.

The NiFe oxyhydroxide unit cell used in the calculations is depicted in Fig. 2 and is representative of 2D, periodic, single layers of the oxyhydroxide material separated by vacuum. The interlayer hydrogen-bonding interactions, which have been explored previously (22), do not qualitatively change the electronic structure properties of interest herein (see *SI Appendix*, Fig. S1). Solvent molecules and ions, which are known to intercalate between layers of the film, should further attenuate layer–layer interactions (23) and are expected to have only a minor influence on the electronic structure of the material. The system with 25% Fe doping was modeled by replacing one Ni site in the unit cell with Fe. Geometries of different redox and protonation states of the layers were optimized at the DFT+U level of theory (17, 24), followed by a single-point energy calculation with the hybrid functional of Perdew–Burke–Ernzerhof, PBE0 (25, 26) (see *SI Appendix* for details). The proton-coupled oxidation, or net dehydrogenation, of the oxyhydroxide materials was modeled by systematically removing H atoms from the layers. The Ni-only materials studied herein are denoted $Ni_4O_8H_n$, where n = 0–8. Representative examples for n = 8 and 0 correspond to $Ni(OH)_2$ and NiO_2, respectively. Similarly, the different redox and protonation states of the 25% Fe-doped materials are denoted $Ni_3Fe_1O_8H_n$ (n = 0–8). At each value of n, the lowest-energy hydrogen configuration found was used in our analyses. The experimentally studied materials have a mixture of hydrogen configurations and Fe site positions that may lead to heterogeneities in oxidation and spin states that are not accessible via periodic calculations based on a small unit cell.

The computed proton-coupled redox potentials for the various reactions are given in Table 1. All of the reported potentials in Table 1 are calculated relative to the experimentally determined $Ni^{2+/3+}$ potential for the Ni-only $Ni_4O_8H_n$ system (i.e., n = 8 to n = 4) because only the computed relative potentials are expected to be quantitatively reliable. Specifically, the redox potentials are calculated from the expression

$$E^{o} = -\frac{\Delta U^{o}}{nF} + \frac{\Delta U^{o}_{ref}}{n'F} + E^{o}_{ref} = -\frac{\Delta U^{o}}{nF} + E_{corr},$$

where F is the Faraday constant, ΔU^{o} is the electronic energy change associated with $MO_xH_{y-n} \rightarrow MO_xH_y$ (the reaction of interest), ΔU^{o}_{ref} is the electronic energy change associated with $MO_xH_{y'-n'} \rightarrow MO_xH_{y'}$ (the reference reaction), and E^{o}_{ref} is the experimentally determined reduction potential for the reference reaction. The correction factor $E_{corr} = E^{o}_{ref} + (\Delta U^{o}_{ref}/n'F)$ is the difference between the experimental and calculated reduction potentials for the reference reaction. This procedure is based on a thermodynamic scheme that eliminates the energy of the H_2 molecules and ensures cancellation of the majority of the translational, rotational, and vibrational entropic contributions. More details about this procedure are provided in the *SI Appendix*. The aqueous solvent environment and displacement of protons by

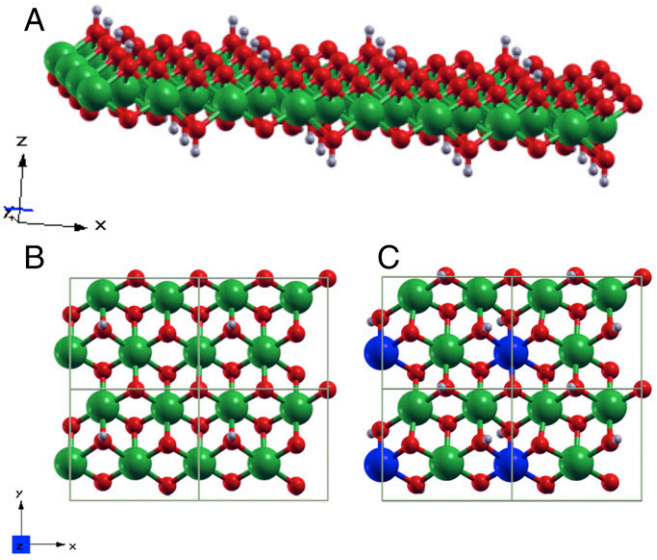

Fig. 2. Single-layer NiFe oxyhydroxide, composed of Ni (green), O (red), H (gray), and Fe (blue) for (*A*) the undoped Ni oxyhydroxide, $Ni_4O_8H_2$, viewed from the side; (*B*) viewed from above the surface; (*C*) the NiFe oxyhydroxide doped 25% with Fe, $Ni_3Fe_1O_8H_4$, viewed from above the surface. *B* and *C* depict the unit cell that is periodically replicated in two dimensions for all calculations, with varying numbers of hydrogens.

Table 1. Proton-coupled redox potentials (V vs. NHE) for pure $Ni_4O_8H_n$ and 25% Fe-doped $Ni_3Fe_1O_8H_n$ calculated with PBE0

$Ni_4O_8H_n$			$Ni_3Fe_1O_8H_n$		
Reactant	Products	*E*	Reactant	Products	*E*
8H	6H + H_2	0.52	8H	7H + 0.5 H_2	−0.72
8H	4H + 2 H_2	0.53*	7H	6H + 0.5 H_2	0.60
8H	2H + 3 H_2	0.59	7H	5H + 1 H_2	0.52
6H	4H + H_2	0.54	7H	4H + 1.5 H_2	0.55
4H	2H + H_2	0.73	7H	3H + 2 H_2	0.63
2H	0H + H_2	0.92	7H	2H + 2.5 H_2	0.60
			7H	1H + 3 H_2	0.69
			7H	0H + 3.5 H_2	0.73

In the reactant and products, *n*H denotes the stoichiometry of the film. Plots of the relative formation free energies versus potential for both the pure Ni and the Fe-doped systems are given in *SI Appendix*, Fig. S2 to facilitate the determination of the most stable stoichiometries at pH 14.
*This potential is set equal to the experimental value at pH 14, and all other reported potentials are calculated relative to this value. The analogous table using the 8H → 2H + 3 H_2 reaction as the reference is given as *SI Appendix*, Table S4, shifting all potentials downward by 0.06 V.

intercalated cations are not considered explicitly but are assumed to exert an approximately similar effect on all species. As a result, these effects approximately cancel in the referencing scheme, which involves the calculation of only relative potentials. Recent data suggest that solvated ions could have a kinetic influence (27, 28), but kinetic issues are not addressed in these calculations.

Our results indicate the importance of using hybrid functionals for these types of systems. The relative redox potentials obtained from PBE+*U* calculations are systematically lower than those obtained from both PBE0 calculations and the CV experiments (*SI Appendix*, Table S3). The PBE+*U* method, as implemented with a single value of *U* for each metal, does not provide reliable redox thermodynamic properties for this material, most likely because multiple oxidation states of the same metals are present (22, 29–31). Although computationally expensive, the use of the hybrid PBE0 functional avoids the parameterization necessary for the quantitatively reliable implementation of the PBE+*U* method for this type of system. The use of PBE0 is further motivated by recent calculations suggesting that the mixing fraction of exact exchange in global hybrid functionals should be chosen to be the inverse of the dielectric constant (32–34). The high-frequency dielectric constant was computed to be ∼3.5 for bulk $Ni(OH)_2$ (35), suggesting a fraction of exact exchange of 0.29, comparable to the fraction of 0.25 for PBE0.

The two redox processes observed experimentally in the Ni-only oxyhydroxide material (Fig. 1, black trace) are consistent with the computed potentials in Table 1. The quasi-reversible feature in the experimental CV centered at 0.53 V vs. NHE is attributed to complete oxidation of Ni^{2+} to Ni^{3+}, corresponding to 4 H^+/4 e^- oxidation of the $Ni_4O_8H_8$ unit cell (i.e., one electron per nickel), leading to the reference of 8H → 4H + 2 H_2 used in Table 1. However, literature data (36, 37) also provide evidence that this feature could correspond to 6 H^+/6 e^- oxidation of the $Ni_4O_8H_8$ unit cell (i.e., 1.5 electrons per nickel), which would suggest a reference of 8H → 2H + 3 H_2. Given this uncertainty, the proton-coupled redox potentials were also calculated with the reference reaction corresponding to 8H → 2H + 3 H_2, as given in *SI Appendix*, Table S4. Because this different reference simply shifts all redox potentials downward by 0.06 V, the qualitative trends and conclusions do not change with the use of a different reference. It is further noted that these calculations provide only thermodynamic information and do not address kinetic complexity, such as that evident in the relatively large splitting between the anodic and cathodic peaks in the CV (Fig. 1). As indicated by Table 1, the proton-coupled oxidations of the layer corresponding to 8H → 6H + H_2 and 6H → 4H + H_2 are predicted to occur at nearly the same potential. The next redox event observed experimentally is the onset of catalytic current, together with the small redox feature at the foot of the wave. The computations suggest these features correlate with further oxidation of the film (4H → 2H + H_2), computed to occur at 0.73 V (Table 1).

Calculations on the $Ni_3Fe_1O_8H_n$ system predict that Fe will be in the Fe^{3+} state at open circuit, corresponding to $n = 7$ (i.e., 7H). Specifically, the $Fe^{2+/3+}$ redox potential (8H → 7H + 0.5 H_2) was computed to be −0.72 V, which is lower than that accessible experimentally. The first (and only) experimentally observed redox event is associated with the onset of catalytic current (Fig. 1, red trace), and the calculations suggest that multiple proton-coupled oxidations are viable at the observed potential. Accessible states range from $n = 6$ to $n = 2$, with calculated potentials spanning 0.52–0.63 V (Table 1). The metal-ion oxidation states and electronic structure features of these catalyst redox states will be elaborated below.

Ni and Fe Oxidation States upon Proton-Coupled Oxidation. The determination of oxidation states is notoriously challenging, particularly in periodic calculations. We used the site-specific magnetizations, namely the difference in spin-up and spin-down densities localized on Ni and Fe, as signatures of different oxidation states. Magnetizations have also been used recently to analyze the 3D periodic solid β-NiOOH (19). Whereas other quantitative methods for inferring integer metal oxidation states in the solid state have been developed (38, 39), the use of

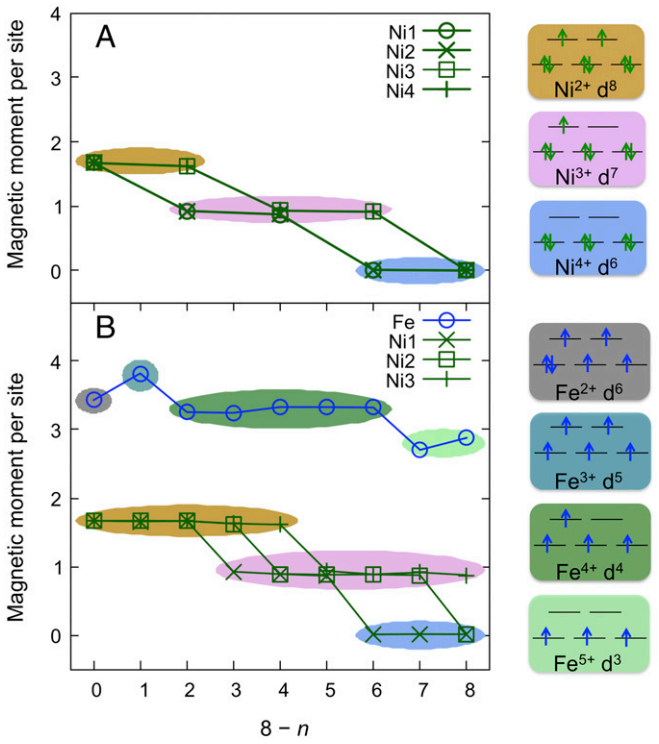

Fig. 3. Calculated magnetic moments of each metal center in the unit cell vs. 8 − *n* for (*A*) pure $Ni_4O_8H_n$ and (*B*) Fe-doped $Ni_3Fe_1O_8H_n$. The radii over which the spin densities were integrated were determined by Quantum ESPRESSO. Oxidation states of each metal center are color-coded as follows: Ni^{2+} (gold), Ni^{3+} (pink), Ni^{4+} (blue), Fe^{2+} (gray), Fe^{3+} (teal), Fe^{4+} (dark green), and Fe^{5+} (light green). Accompanying electronic structure diagrams are idealized and neglect possible quasi-Jahn–Teller distortions.

site-specific magnetizations provides a clear qualitative picture for this system. To validate this approach, we carried out additional calculations with maximally localized Wannier functions (38), which provide results in agreement with those inferred from site-specific magnetizations (*SI Appendix*, Table S6). Furthermore, as shown in *SI Appendix*, Table S2, the metal–oxygen bond lengths correlate with the computed formal oxidation states.

The following discussion presents a systematic analysis of the computed oxidation states as a function of the H stoichiometry and thereby connects them to the proton-coupled redox potentials described above. For Ni, the 2+, 3+, and 4+ oxidation states correspond to 2, 1, and 0 unpaired electrons, respectively, localized on a given Ni atom. Fe oxidation states from 2+ to 5+ were observed in the studied range of H stoichiometries. The PBE0 calculations suggest that the ground state for each Fe species is high spin, in accordance with available experimental data for Fe^{3+} (18). The calculations indicate that Fe^{4+} is also high spin, which has not been resolved experimentally, but may arise from the constraints and environment imposed by the extended lattice. Moreover, Mn^{3+}, which is isoelectronic to Fe^{4+}, in the analogous NiMn layered double hydroxide has been found to be high spin (40). The computed magnetizations and corresponding oxidation states for each metal site in the unit cell of the periodic system are depicted in Fig. 3. Whereas NiO_2 and Fe^{5+}-containing systems were investigated computationally and are represented in Fig. 3, neither is accessible under experimental conditions owing to their high potentials.

For the $Ni_4O_8H_n$ material shown in Fig. 3*A*, sequential proton-coupled oxidations of the layer result in oxidations of the Ni sites from entirely Ni^{2+} in $Ni_4O_8H_8$ to entirely Ni^{4+} in $Ni_4O_8H_0$. In the intermediate case of $Ni_4O_8H_4$, there are four magnetically equivalent Ni^{3+} sites. In the systems defined by $n = 6$ and $n = 2$ (6H and 2H), a coexistence of different Ni oxidation states is observed. In $Ni_4O_8H_2$, which is expected to be catalytically active, magnetizations characteristic of Ni^{4+} and Ni^{3+} are observed for two sites each. As expected, the deprotonation of an oxygen is accompanied by oxidation of one of the metal centers bonded to that oxygen.

The same analysis of site-specific magnetizations for the Fe-doped systems is depicted in Fig. 3*B*. As noted above, the open-circuit $Ni_3Fe_1O_8H_7$ state has three Ni^{2+} sites and one Fe^{3+} site in the unit cell. Upon proton-coupled oxidation, Fe is oxidized to Fe^{4+} before any of the Ni^{2+} sites are oxidized. Furthermore, Fe^{4+} is observed in stoichiometries from $n = 6$ to $n = 2$ (6H to 2H), the same range of compositions that can be present under catalytic conditions based on the calculated redox potentials in Table 1. This observation is in accordance with the *operando* Mössbauer spectroscopic identification of Fe^{4+} (18). At the Fe-doped oxyhydroxide stoichiometry, $Ni_3Fe_1O_8H_4$, the Fe^{4+} site exists in conjunction with one Ni^{2+} site and two Ni^{3+} sites, in contrast to the uniformly 3+ oxidation states in the pure Ni oxyhydroxide. This observation indicates charge transfer occurring from Fe to Ni in the working catalyst, which is further elucidated in the electronic structure analysis below.

Optoelectronic Properties of NiFe Oxyhydroxide. Thin films of $Ni(OH)_2$ or Fe-doped $Ni(OH)_2$ were prepared on transparent FTO (fluorine-doped tin oxide) electrodes to analyze the catalyst via spectroelectrochemistry. UV-visible spectra were acquired while holding the catalyst-coated electrode at different applied potentials (Fig. 4; see the *SI Appendix* for details). A prominent spectroscopic feature corresponding to the band-edge absorption develops for both the Ni and NiFe catalysts upon increasing the potential (Fig. 4 *B* and *D*). The absorption at 2.5 eV, depicted as a function of applied potential in Fig. 4 *A* and *C* (filled circles; right *y* axis), illustrates that the optical changes are directly correlated with the redox changes in the catalyst.

The pure Ni and Fe-doped materials exhibit qualitatively different optoelectronic behavior. For the $Ni(OH)_2$ material, the film darkens as NiOOH is formed, starting at ~0.53 V (Fig. 4 *A* and *B*), and then further darkens as the potential is raised to the onset of catalysis. Within the catalytic wave, the absorption

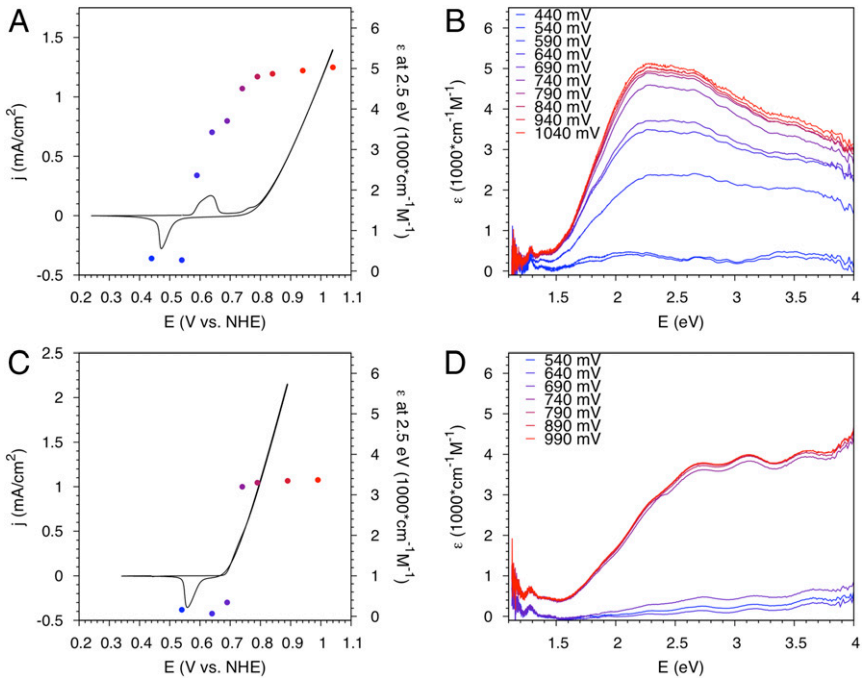

Fig. 4. CVs (*Left*) and UV/vis spectra (*Right*) of the (*A* and *B*) pure Ni and (*C* and *D*) 25% Fe films. Data points in the CVs correspond to the absorbance at 2.5 eV with the same color coding as in the spectra. The UV/vis spectra were obtained at steady state during constant-potential electrocatalysis. Spectroelectrochemistry for intermediate loadings of Fe is shown in *SI Appendix*, Fig. S10.

spectrum is largely independent of potential. Although the calculations suggest that higher redox states should be accessible in the potential range evaluated, rapid water oxidation under these conditions will result in these states not having significant population and/or lifetime. In the 25% Fe-doped material, negligible absorbance changes are evident until the onset of OER activity, corresponding to the first redox feature evident in the CV (Fig. 4 *C* and *D*). The band-edge absorption energy is similar to that of the pure Ni film, beginning at 1.5 ± 0.1 eV. Once again, negligible absorbance changes are observed as the potential is increased into the catalytic wave because higher oxidation states of the catalyst are not attained, owing to rapid water oxidation from such states (41). These observations, in combination with the computed metal-ion redox potentials described above, are consistent with the presence of significant quantities of Fe^{4+} in the steady-state catalyst (18).

To understand the trends in the measured optical gaps, we compared experimental results to the computed fundamental band gaps for each film, as obtained from the differences of the eigenvalues of the valence band maximum (VBM) and the conduction band minimum (CBM) calculated with PBE0 for the pure Ni and Fe-doped systems (*SI Appendix*, Table S7). The band gaps computed with PBE+*U* are almost vanishing for the catalytically relevant states (*SI Appendix*, Figs. S5 and S6), and thus the use of the PBE0 functional is essential to reasonably describe these band gaps. Similar observations were reported for bulk Ni oxyhydroxide (22, 42). The calculated band gaps of both the pure Ni and 25% Fe-doped systems decrease upon proton-coupled oxidation, as observed via spectroelectrochemistry. The observation that pure Ni and Fe-doped thin films have similar absorption onsets is consistent with the similarity in the computed band gaps for these two systems. The calculated fundamental gaps are on the order of ∼1 eV higher than the corresponding optical gaps measured experimentally; however, this discrepancy is not unexpected as the computed values do not include the exciton binding energy, which for NiO is on the order of ∼1 eV (43).

Electronic Structure of NiFe Oxyhydroxide and the Effects of Fe Doping. To elucidate the effect of Fe in the doped oxyhydroxide system, we analyzed the electronic structure of both the Ni and NiFe materials around the Fermi level. The atomic projected density of states (PDOS) for two layered materials, $Ni_4O_8H_2$ and $Ni_3Fe_1O_8H_4$, are shown in Fig. 5 *A* and *E*, respectively. Further breakdowns of the PDOS in Fig. 5 *B–D* and Fig. 5 *F–H* illustrate the electronic structure associated with specific metal atoms and oxidation states and differentiate between bridging hydroxide and oxide ligand states (i.e., states associated with protonated and deprotonated oxygen atoms).

In $Ni_4O_8H_2$, the Ni^{3+} electronic states at the VBM are closer to the Fermi level than are the Ni^{4+} states, and states associated with both Ni^{3+} and Ni^{4+} contribute to the CBM (Fig. 5*B*). Additionally, oxide ligand states are more prevalent than hydroxide ligand states in the CBM composition (Fig. 5*C*). The PDOS plots associated with oxides bound to Ni atoms in different oxidation states are similar (Fig. 5*D*). This similarity is not surprising given that in the figure O–Ni^{3+} refers to states associated with O atoms bound to two Ni^{3+} sites and one Ni^{4+} site, whereas O–Ni^{4+} refers to states associated with O atoms bound to two Ni^{4+} sites and one Ni^{3+} site.

The corresponding analysis of the Fe-doped Ni-oxyhydroxide ($Ni_3Fe_1O_8H_4$) reveals important differences. Fig. 5*F* demonstrates that electronic states associated with Ni^{2+} dominate the VBM, whereas those associated with the dopant Fe^{4+} dominate the CBM. This Fe-to-Ni charge-transfer character is evident in states comprising both the VBM and the CBM. As observed for the Ni-only catalyst, oxide ligand states are more prevalent than hydroxide ligand states in the CBM (Fig. 5*G*). The oxide ligand states in the NiFe material, however, exhibit a distinct metal-coordination dependence. In Fig. 5*H*, O–Ni refers to states of O atoms not bound to Fe, whereas O–Fe^{4+} refers to states of O atoms bound to one Fe site and two Ni sites. States associated with Fe^{4+}-ligated oxides are energetically lower than those associated with oxides ligated to only Ni and thus dominate the CBM.

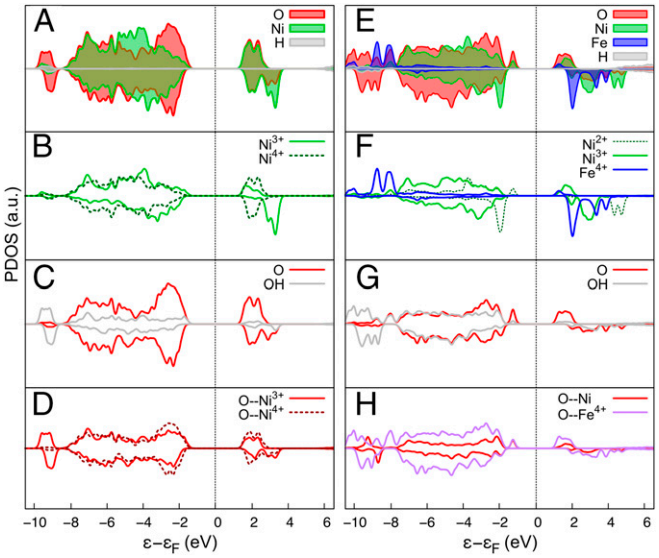

Fig. 5. PDOS analysis of catalytically active species for (*A–D*) pure $Ni_4O_8H_2$ and (*E–H*) doped $Ni_3Fe_1O_8H_4$. In these plots, the α electronic density is positive (up), and the β electronic density is negative (down). In *C* and *G*, O and OH refer to oxide and hydroxide ligand states, respectively.

Conclusion

We have used electronic structure methods and spectroelectrochemistry to characterize the pure Ni and Fe-doped oxyhydroxide OER electrocatalysts. In the Ni-only material, the onset of the OER catalytic current occurs at potentials that generate Ni^{4+}, whereas in the 25% Fe-doped system, a number of redox states, which all contain Fe^{4+}, are thermodynamically accessible at catalytic potentials. The observed dependence of the optical properties on the potential directly corresponds to these predicted changes in the redox states. The electronic structure of the Ni-only and Fe-doped materials reveals that the conduction band minimum is dominated by hybrid Ni-oxide states in the pure Ni system and by Fe-oxide states in the Fe-doped material.

These results have clear implications for the catalytic OER mechanism. For example, water oxidation is commonly proposed to involve nucleophilic attack of water on a high-valent metal oxide species, and the results described herein show that the NiOOH lattice enables facile oxidation of Fe^{3+} to Fe^{4+}. The oxidation to Fe^{4+} may be facilitated by the superior electronic conductivity of the mixed-metal system relative to pure Fe oxyhydroxide (44, 45). Catalytically active sites are likely to be present at edge, corner, or defect sites. Based on the electronic structure results obtained here for the bulk, it is reasonable to extrapolate that Fe-oxide motifs at such sites will exhibit electrophilicity suitable to mediate water oxidation. However, the metal oxidation and spin states at defect sites could differ from those at regular lattice sites. The present results provide an excellent foundation for future efforts to probe this hypothesis.

Materials and Methods

The computational and experimental methodologies used in this work are elaborated in the *SI Appendix*. These methods include the derivation of the calculated proton-coupled redox potentials, details of the various DFT calculations performed, NiFe oxyhydroxide thin-film deposition, and aspects of the spectroelectrochemical experiments. All calculations were performed with Quantum ESPRESSO (46) unless otherwise specified.

ACKNOWLEDGMENTS. This work was supported by the Center for Chemical Innovation of the National Science Foundation (Solar Fuels, Grant CHE-1305124). Z.K.G. acknowledges support from National Science Foundation Partnerships for International Research and Education Grant 1545907.

1. Dau H, et al. (2010) The mechanism of water oxidation: From electrolysis via homogeneous to biological catalysis. *ChemCatChem* 2(7):724–761.
2. Walter MG, et al. (2010) Solar water splitting cells. *Chem Rev* 110(11):6446–6473.
3. Singh A, Spiccia L (2013) Water oxidation catalysts based on abundant 1st row transition metals. *Coord Chem Rev* 257(17):2607–2622.
4. Galán-Mascarós JR (2015) Water oxidation at electrodes modified with earth-abundant transition-metal catalysts. *ChemElectroChem* 2(1):37–50.
5. Hall DE (1985) Alkaline water electrolysis anode materials. *J Electrochem Soc* 132(2): 41C–48C.
6. Trasatti S (1991) Physical electrochemistry of ceramic oxides. *Electrochim Acta* 36(2): 225–241.
7. Corrigan DA (1987) The catalysis of the oxygen evolution reaction by iron impurities in thin film nickel oxide electrodes. *J Electrochem Soc* 134(2):377–384.
8. Park S, Shao Y, Liu J, Wang Y (2012) Oxygen electrocatalysts for water electrolyzers and reversible fuel cells: Status and perspective. *Energy Environ Sci* 5(11):9331–9344.
9. Miles MH (1975) Evaluation of electrocatalysts for water electrolysis in alkaline solutions. *J Electroanal Chem* 60(1):89–96.
10. Lyons MEG, Brandon MP (2008) The oxygen evolution reaction on passive oxide covered transition metal electrodes in aqueous alkaline solution. Part 1-Nickel. *Int J Electrochem Sci* 3:1386–1424.
11. Trotochaud L, Young SL, Ranney JK, Boettcher SW (2014) Nickel-iron oxyhydroxide oxygen-evolution electrocatalysts: The role of intentional and incidental iron incorporation. *J Am Chem Soc* 136(18):6744–6753.
12. Louie MW, Bell AT (2013) An investigation of thin-film Ni-Fe oxide catalysts for the electrochemical evolution of oxygen. *J Am Chem Soc* 135(33):12329–12337.
13. Li Y-F, Selloni A (2014) Mechanism and activity of water oxidation on selected surfaces of pure and Fe-doped NiO_x. *ACS Catal* 4(4):1148–1153.
14. Dionigi F, Strasser P (2016) NiFe-based (oxy)hydroxide catalysts for oxygen evolution reaction in non-acidic electrolytes. *Adv Energy Mater* 6(23):1600621.
15. Gerken JB, Shaner SE, Massé RC, Porubsky NJ, Stahl SS (2014) A survey of diverse earth abundant oxygen evolution electrocatalysts showing enhanced activity from Ni–Fe oxides containing a third metal. *Energy Environ Sci* 7(7):2376–2382.
16. Friebel D, et al. (2015) Identification of highly active Fe sites in (Ni,Fe)OOH for electrocatalytic water splitting. *J Am Chem Soc* 137(3):1305–1313.
17. Anisimov VI, Zaanen J, Andersen OK (1991) Band theory and Mott insulators: Hubbard *U* instead of Stoner *I*. *Phys Rev B Condens Matter* 44(3):943–954.
18. Chen JYC, et al. (2015) Operando analysis of NiFe and Fe oxyhydroxide electrocatalysts for water oxidation: Detection of Fe^{4+} by Mössbauer spectroscopy. *J Am Chem Soc* 137(48):15090–15093.
19. Conesa JC (2016) Electronic structure of the (undoped and Fe-doped) NiOOH O_2 evolution electrocatalyst. *J Phys Chem C* 120(34):18999–19010.
20. Trotochaud L, Ranney JK, Williams KN, Boettcher SW (2012) Solution-cast metal oxide thin film electrocatalysts for oxygen evolution. *J Am Chem Soc* 134(41):17253–17261.
21. Chen JYC, Miller JT, Gerken JB, Stahl SS (2014) Inverse spinel $NiFeAlO_4$ as a highly active oxygen evolution electrocatalyst: Promotion of activity by a redox-inert metal ion. *Energy Environ Sci* 7(4):1382–1386.
22. Tkalych AJ, Yu K, Carter EA (2015) Structural and electronic features of β-$Ni(OH)_2$ and β-NiOOH from first principles. *J Phys Chem C* 119(43):24315–24322.
23. Tessier C, Haumesser P, Bernard P, Delmas C (1999) The structure of $Ni(OH)_2$: From the ideal material to the electrochemically active one. *J Electrochem Soc* 146(6):2059–2067.
24. Anisimov VI, Aryasetiawan F, Lichtenstein A (1997) First-principles calculations of the electronic structure and spectra of strongly correlated systems: The LDA+*U* method. *J Phys Condens Matter* 9(4):767.
25. Perdew JP, Ernzerhof M, Burke K (1996) Rationale for mixing exact exchange with density functional approximations. *J Chem Phys* 105(22):9982–9985.
26. Adamo C, Barone V (1999) Toward reliable density functional methods without adjustable parameters: The PBE0 model. *J Chem Phys* 110(13):6158–6170.
27. Hunter BM, et al. (2014) Highly active mixed-metal nanosheet water oxidation catalysts made by pulsed-laser ablation in liquids. *J Am Chem Soc* 136(38):13118–13121.
28. Hunter BM, Hieringer W, Winkler JR, Gray HB, Müller AM (2016) Effect of interlayer anions on [NiFe]-LDH nanosheet water oxidation activity. *Energy Environ Sci* 9: 1734–1743.
29. Kulik HJ, Cococcioni M, Scherlis DA, Marzari N (2006) Density functional theory in transition-metal chemistry: A self-consistent Hubbard *U* approach. *Phys Rev Lett* 97(10):103001.
30. Chen J, Wu X, Selloni A (2011) Electronic structure and bonding properties of cobalt oxide in the spinel structure. *Phys Rev B* 83(24):245204.
31. Kulik HJ, Marzari N (2011) Accurate potential energy surfaces with a DFT+*U*(R) approach. *J Chem Phys* 135(19):194105.
32. Skone JH, Govoni M, Galli G (2014) Self-consistent hybrid functional for condensed systems. *Phys Rev B* 89(19):195112.
33. Brawand NP, Vörös M, Govoni M, Galli G (2016) Generalization of dielectric-dependent hybrid functionals to finite systems. *Phys Rev X* 6(4):041002.
34. Skone JH, Govoni M, Galli G (2016) Nonempirical range-separated hybrid functionals for solids and molecules. *Phys Rev B* 93(23):235106.
35. Hermet P, et al. (2011) Dielectric, magnetic, and phonon properties of nickel hydroxide. *Phys Rev B* 84(23):235211.
36. Merrill M, Worsley M, Wittstock A, Biener J, Stadermann M (2014) Determination of the "NiOOH" charge and discharge mechanisms at ideal activity. *J Electroanal Chem* 717–718:177–188.
37. Smith RDL, Berlinguette CP (2016) Accounting for the dynamic oxidative behavior of nickel anodes. *J Am Chem Soc* 138(5):1561–1567.
38. Sit PH, Car R, Cohen MH, Selloni A (2011) Simple, unambiguous theoretical approach to oxidation state determination via first-principles calculations. *Inorg Chem* 50(20): 10259–10267.
39. Jiang L, Levchenko SV, Rappe AM (2012) Rigorous definition of oxidation states of ions in solids. *Phys Rev Lett* 108(16):166403.
40. Giovannelli F, et al. (2012) Magnetic properties of Ni(II)–Mn(III) LDHs. *Mater Chem Phys* 137(1):55–60.
41. Görlin M, et al. (2016) Oxygen evolution reaction dynamics, Faradaic charge efficiency, and the active metal redox states of Ni–Fe oxide water splitting electrocatalysts. *J Am Chem Soc* 138(17):5603–5614.
42. Zaffran J, Caspary Toroker M (2016) Benchmarking density functional theory based methods to model NiOOH material properties: Hubbard and van der Waals corrections vs hybrid functionals. *J Chem Theory Comput* 12(8):3807–3812.
43. Rödl C, Bechstedt F (2012) Optical and energy-loss spectra of the antiferromagnetic transition metal oxides MnO, FeO, CoO, and NiO including quasiparticle and excitonic effects. *Phys Rev B* 86(23):235122.
44. Burke MS, Enman LJ, Batchellor AS, Zou S, Boettcher SW (2015) Oxygen evolution reaction electrocatalysis on transition metal oxides and (oxy)hydroxides: Activity trends and design principles. *Chem Mater* 27:7549–7558.
45. Zou S, et al. (2015) Fe (oxy)hydroxide oxygen evolution reaction electrocatalysis: Intrinsic activity and the roles of electrical conductivity, substrate, and dissolution. *Chem Mater* 27(23):8011–8020.
46. Giannozzi P, et al. (2009) QUANTUM ESPRESSO: A modular and open-source software project for quantum simulations of materials. *J Phys Condens Matter* 21(39):395502.